Review of Scientific Instruments

RESEARCH ARTICLE | JUNE 12 2026

A white beam spin echo interferometer for neutron orbital angular momentum generation

Niels Geerits; Simon Hack; Lara Brukner; Ad van Well; Steven R. Parnell; Hartmut Abele; Stephan Sponar

Rev. Sci. Instrum. 97, 065211 (2026)
https://doi.org/10.1063/5.0321755

Review of Scientific Instruments | ARTICLE | pubs.aip.org/aip/rsi

A white beam spin echo interferometer for neutron orbital angular momentum generation

Cite as: Rev. Sci. Instrum. 97, 065211 (2026); doi: 10.1063/5.0321755
Submitted: 9 January 2026 • Accepted: 25 May 2026 •
Published Online: 12 June 2026

Niels Geerits,[1,a)] Simon Hack,[1] Lara Brukner,[1] Ad van Well,[2] Steven R. Parnell,[2,3] Hartmut Abele,[1] and Stephan Sponar[1,b)]

AFFILIATIONS

[1] Atominstitut, Technische Universität Wien, Stadionallee 2, 1020 Vienna, Austria
[2] Faculty of Applied Sciences, Delft University of Technology, Mekelweg 15, Delft 2629JB, The Netherlands
[3] ISIS, Rutherford Appleton Laboratory, Chilton, Oxfordshire OX11 0QX, United Kingdom

[a)] **Author to whom correspondence should be addressed:** niels.geerits@tuwien.ac.at
[b)] **Electronic mail:** stephan.sponar@tuwien.ac.at

ABSTRACT

The broadband resonant spin echo interferometer, Coherent Averaging Neutron Instrument for Spin-echo Interferometry and fUndamental Science (CANISIUS), is presented. CANISIUS is located at the 250 kW Training, Research, Isotopes, General Atomics research facility of the Atominstitut, TU Wien, Austria. It is built in a versatile way, such that it can be operated in both a continuous broadband beam and a pulsed time of flight beam. This versatility also extends to the modes available to the instrument, such as neutron resonant spin echo, spin echo (modulated) small angle neutron scattering, and coherent averaging to produce structured wavefunctions for scattering. The instrument may also be used as an interferometer, to probe fundamental questions in quantum mechanics. In this paper, we detail both the continuous and time of flight options of the instrument. In addition, we demonstrate the applicability of our interferometer to ultra small angle scattering in a white beam. Finally, we demonstrate a new spin echo interferometry tool, which uses incomplete recombination of the two path states to generate composite wavefunctions with special structure. In particular, we show that this method produces neutron wavefunctions that exist in a superposition of two quantum mechanical orbital angular momentum modes, $\ell = \pm 1$. We illustrate that just as this method can be used to generate certain structured waves, it may also be used to characterize the structure of the input wavefunction.

I. INTRODUCTION

Neutron interferometry is a powerful and established tool for addressing a variety of scientific challenges from exploring quantum state entanglement in massive particles[1,2] and inertial effects on quantum particles, such as gravitationally induced interference (the Colella Overhauser Werner, or COW, experiment),[3] the Sagnac effect,[4,5] and the Mashhoon effect,[6,7] to nuclear physics questions by measuring scattering cross sections to high precision.[8] Furthermore, grating interferometers[9,10] have been applied to sophisticated imaging techniques such as phase[11–13] and dark-field imaging.[14] Finally, it has been argued that neutron interferometers may be used to create complex structured waves by coherent averaging.[15,16] This method is particularly useful for producing vortex neutrons,[16–18] which carry Orbital Angular Momentum (OAM)[19–21] and may have unique scattering properties.[22–24] Furthermore, OAM represents an additional quantum mechanical degree of freedom, which is useful for quantum information and contextuality experiments.

The most well-known type of neutron interferometer is made from a perfect silicon crystal in triple Laue configuration;[25] however, other methods have been established as well, such as supermirror based approaches[26] and magnetic refraction based approaches.[27] Neutron spin echo[28] techniques, which use the latter method, have been particularly successful. The classic spin echo technique, resonant spin echo,[29] and "Modulation of Intensity Emerging from Zero Effort" (MIEZE)[30] interfere the two neutron spin states in time, which makes these techniques particularly sensitive to dynamic effects, such as those observed in inelastic scattering. In addition, MIEZE has even been applied to observe violations of Bell's inequality.[31,32] In 1978, Pynn proposed a technique to apply spin echo to ultra small angle scattering, by inclining the magnetic field regions with respect to the direct beam.[33] About two decades later, Rekveldt proposed to utilize shaped poleshoes in addition to foil flippers to increase the usable field integral.[34,35] Over time, the technique became known as spin echo small angle neutron scattering (SESANS). This method splits and later focuses the two spin states transversely, which makes the instrument sensitive to structure along the refraction direction (defined by the inclination of the magnetic field region).[27] In recent years, many of the famous neutron interferometry experiments, such as the COW experiment[36,37] and tests of quantum entanglement,[38,39] have been carried out with spin-echo type interferometers. In addition, these interferometers have a few advantages over perfect crystal interferometers, such as the ability to accept a large, broadband, and wide divergence beam. As a result, spin-echo interferometers have a higher usable flux. In addition, this class of interferometer is not as sensitive to temperature variations and vibrations. The most obvious disadvantage is the microscopic path separation (10 nm to 10 μm); consequently, the paths can usually not be manipulated separately. Nonetheless, the area spanned by the two paths of a spin-echo interferometer is similar to that of a single crystal interferometer. In addition, it is simpler to produce structured wavefunctions by coherent averaging with spin echo interferometers, due to the possibility of a modular design, which allows for an arbitrary number of beam splitters and paths in a single instrument.

In this paper, we report on the new broadband spin-echo interferometer, Coherent Averaging Neutron Instrument for Spin-echo Interferometry and fUndamental Science (CANISIUS), designed to investigate the properties of vortex neutrons carrying non-zero OAM. CANISIUS follows similar design doctrines as the Offspec[40] and Larmor[41,42] instruments at the ISIS neutron source, as well as the instruments developed at TU Delft.[43] That is to say, CANISIUS uses adiabatic RF flippers[44] to ensure broadband efficiency and is built in a modular way so that it can be applied to a variety of different modes [SESANS, Spin Echo Modulated Small Angle Neutron Scattering (SEMSANS),[45] Neutron Resonant Spin Echo (NRSE), and Modulation of Intensity Emerging from Zero Effort (MIEZE)]. In addition, CANISIUS can quickly change between a continuous white beam and a pulsed beam for time of flight (ToF). Here, we report the design and efficiency of the adiabatic RF-flippers and the instrument, the interference patterns produced by the instrument in broadband and time of flight (ToF) SESANS modes. and, finally, discuss production and investigation of vortex neutrons.

II. METHODS

A. Instrument overview

A three dimensional render of the CANISIUS instrument in a SESANS configuration is shown in Fig. 1. CANISIUS is situated at the white beamline of the Atominstitut (TU Wien) 250 kW reactor. The instrument can be operated in either a continuous broadband or two distinct ToF modes. A standard mechanical chopper is used for the regular ToF mode. The second mode is enabled by a spin chopping system, which is made possible since the beam is initially polarized by double reflection from a pair of m = 4 single flat substrate Fe/Si supermirrors; this allows the beam to be chopped by inserting a broadband spin flipper between the two mirrors, which

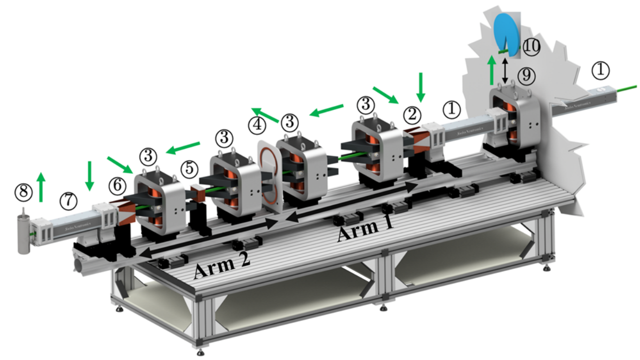

FIG. 1. Render of the CANISIUS instrument configured for white beam SESANS. The beam propagates from right to left. First, the beam is polarized by double reflection from two single substrate m = 4 polarizing supermirrors (1). Next, the polarization is adiabatically rotated by 90° by a v-coil (2). The beam then passes through a pair (arm 1) of adiabatic RF flippers with parallelogram shaped poleshoes, which act as the first beam splitter and mirror (3). A field stepper is positioned between the first and second pairs (arm 2) of RF flippers, to facilitate a fast non-adiabatic field transition from arm 1 to arm 2 (4). The samples of various types may be inserted right before the field stepper. The second arm of RF flippers serves effectively as a mirror and beam splitter to recombine the split beams. Between the last two RF flippers, the beam is passed through a precession coil (5), which manipulates the spin phase to measure the spin echo curve. Finally, before the spin is selected by the last polarizing supermirror (7), the neutrons pass through a final v-coil facilitating another adiabatic 90° rotation (6). Neutrons passing the polarizing supermirror are detected by a high-efficiency ^{3}He counting tube. In addition to the usual continuous mode of operation, the CANISIUS instrument can also be operated in ToF mode. For this purpose, two chopper device are available: a conventional mechanical chopper (10) as well as a spin-chopper system (9), consisting of an RF flipper in combination with the pre-polarizer, that is, the very first supermirrors (1). The length of the instrument, given by the distance between chopper (9 and 10) and detector (8), is 3 m. A hypothetical polarization vector and the resulting precession are shown at various points in the setup using a green arrow. The dephasing is not depicted.

can be pulsed.[46,47] These supermirrors were produced by SwissNeutronics and are cited of having a polarizing power of 0.99 s.[48] Due to the cutoff of the supermirrors, the available wavelength range is 2 – 6Å, with a peak at 2.5Å (see Fig. 4). After the double reflection polarizer, the beam is passed through a v-coil, which adiabatically rotates the neutron spin around the propagation axis from vertical to horizontal. In the first arm of the instrument, which consists of a pair of adiabatic RF flippers,[49] the two spin states are separated longitudinally (standard NRSE) and if parallelogram shaped poleshoes are employed also transversely (SESANS). The second arm with equal but opposite field of the first arm recombines the spin states. Spatial overlap between the two spin states is ultimately measured by a spin projective measurement, which, in practice, is enabled by a v-coil and a supermirror. An additional closed coil in arm 2 allows variation of the phase between the two spin states. The polarizers and RF coils define the maximal beam size to 7 × 20 mm^2. This beam size is used for most measurements described here, except when otherwise specified. These components also define the maximal divergence of 2 mrad at the detector position, provided that no scattering occurs between the first polarizer and the detector. At the sample position, the divergence can be much higher, up to 8 mrad, while the acceptance between the sample position and the detector is estimated to be 6 mrad. A calibration wedge can be inserted between the yoke and the poleshoe to change and calibrate the angle of the poleshoes by up to $\pm 5^{\circ}$. This gives some more flexibility to tune the transverse spin state separation; however, its primary purpose is to enable the new coherent averaging mode, to produce structured neutron waves. If both arms of the interferometer are operated at a different poleshoe angle, the instrument fails to focus the spin states transversely. As a result, some residual separation is left between the spin states. As shown in Sec. II E, this residual separation induces a structured wave with OAM. The residual separation may also be scanned, thus allowing one to measure the correlation between the spin up and down wavefunctions, similar to what is described in Ref. 50. On average, over the entire wavelength band, the polarization of the instrument in the non-echo mode (RF system and v-coils turned off; nonetheless, the static fields are matched to the 1.4 MHz resonance), in which there should be no spin precession, is 0.904. The RF coils are matched to the output impedance of the amplifiers for operation at 1.4 MHz; however, the coils may also be operated in resonant mode (ToF or monochromatic), in which case they can be operated at any frequency between 10 kHz and 5 MHz, since the power requirements are low (1–2 W) and the amplifiers are equipped to handle up to 400 W of reflected power. In the following subsections, the adiabatic RF flippers, SESANS, the ToF modes, and the coherent averaging mode will be discussed in more detail.

B. Adiabatic RF spin flippers

In this subsection, we provide a detailed overview of the design of CANISIUS' RF flipper system. An RF flipper is depicted in Fig. 2, for three different poleshoe configurations, square for NRSE and MIEZE, parallelogram for SESANS and SEMSANS, and tilted parallelogram for coherent averaging. The poleshoes in addition to the magnetic cores were machined from soft iron and subsequently heat treated. The yokes were machined from construction steel. The coils of 400 windings each are situated around each magnetic core and create a vertical field with a shape given by the poleshoes. The gap between the poleshoes is 30 mm, in which the RF system is situated [Fig. 2(d)]. This RF system consists of an aluminum housing containing an 80 mm long RF coil with a diameter of 20 mm, which creates a longitudinal RF field, and a vertical gradient coil, which has minimal winding density in the center and increases toward in the ends of the coil. The RF coil consists of 2 mm copper tubing (inner diameter 1.5 mm) wound on a PEEK (Polyether ether ketone) bobbin and encased in Kapton foil to prevent arcing. A G12 coolant cool rate of 250 ml/minis pumped through the tubing, to facilitate heat transport, and the coolant is cooled to 3 °C by a secondary loop connected to a chiller. Matching of the RF coils to the amplifier output is done capacitively for a single frequency, 1.4 MHz. Mica capacitors were used for their high stability and low loss at typical NRSE frequencies. In adiabatic flipping mode, roughly 60 W are dissipated in each coil, in addition to 40 W in each gradient coil. In resonant flipping mode, only 1–2 W are required depending on the frequency; hence, in this mode, matching between load and amplifier is not necessary. The efficiency of a single adiabatic RF flipper is shown in Fig. 3, which is determined by measuring the polarization in a non-precessing mode (i.e., v-coil turned off) and then normalizing said polarization by the instrument spin transport efficiency, 0.904. The polarization is calculated using the well-known formula,

$$P = \frac{I_{+} - I_{-}}{I_{+} + I_{-}}, \tag{1}$$

where I_{+} is the intensity of the spin state aligned to the analyzing direction (i.e., when the flipper is turned on) and I_{-} is the opposite spin state. Figure 3 demonstrates that our RF flippers have a constant flip efficiency over the entire wavelength band indicating a good adiabaticity of the flippers. A weighted average efficiency of 0.977 can

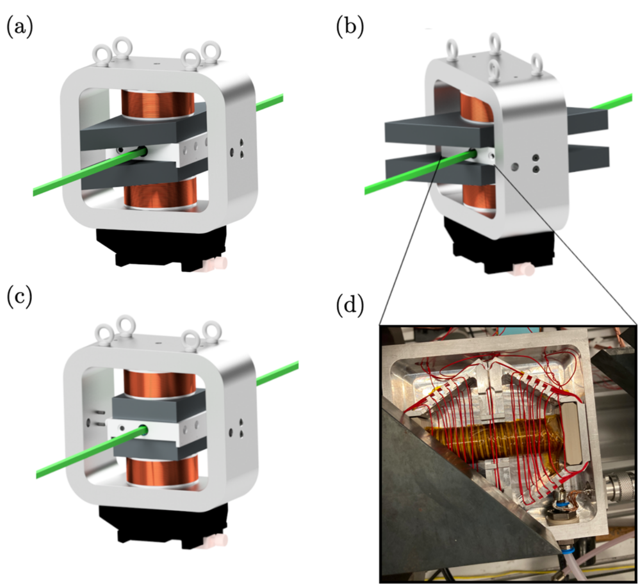

FIG. 2. Render of the adiabatic RF spin flippers with parallelogram shaped poleshoes at 45° (a), 45° ± 5° (b), and 90° in (c). The photograph in (d) shows a top-view of one RF coil partly taken out of the parallelogram shaped poleshoes for demonstration purposes to see the water cooled RF coil, the gradient field coil, as well as the inlet of the coolant and the electrical conducting.

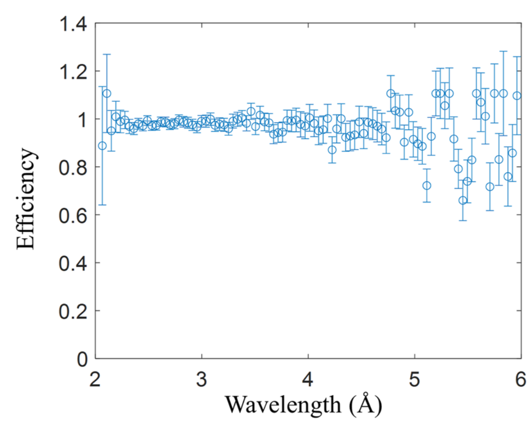

FIG. 3. Flipping efficiency of one adiabatic RF flipper, running at 1.4 MHz, plotted against wavelength. The plot was produced using the ToF technique. This is calculated using ToF spectra with the flipper on and off. The displayed result is normalized by the instrument efficiency of 0.904. The weighted average of the flipping efficiency over the entire spectrum is 0.977.

be extracted from the data shown in Fig. 3. This is comparable to some other adiabatic RF flipper designs.[51] However, we note that flipping efficiency of 99% is possible with similar design.[52] In some other designs, efficiencies of up to 99.9% have been reported.[53]

C. Time of flight options

CANISIUS has two options available for producing a pulsed beam. The first is a Fermi like chopper, which consists of stacked, short, straight, cadmium lined channels, which is spun at 50 Hz, resulting in an effective pulse frequency of 100 Hz. The second method uses an RF flipper positioned between the two polarizing supermirrors. In this case, the two mirrors are oriented to select opposite spins, so that when the flipper is off, no beam is transmitted into the instrument. In resonant mode, the phase accumulated by a neutron in the flipper is given by

$$\alpha = \gamma B_{RF} t, \tag{2}$$

where γ is the gyromagnetic moment of the neutron, B_{RF} is the field strength, and t is the time for which the particle is exposed to the field. Hence, if the RF pulse time is much shorter than the flight time through the device of the fastest neutron, then this phase is wavelength independent. Therefore, to produce a pulsed beam, the RF flipper is simply shortly pulsed in resonant mode, which flips all neutrons that are in the RF coil at the time of the pulse. These neutrons can then be transmitted through the instrument and to the detector. This RF flipper is designed equivalently to the others described in Sec. II B, with the exception of the gradient coil, since this is not required. The RF field pulse length is 5 μs, ten times shorter than the flight time of 2.5Å neutrons through the RF coil. This corresponds to seven cycles of the RF field at 1.4 MHz. However, due to the circuit being tuned to resonance, the coil faces a significant ringdown, which causes the RF field to persist for up to 25 μs per pulse. This is similar to the transit time of 2.5Å neutrons through the coil. As a result, the measured TOF spectra may undersample faster neutrons compared to slow neutrons. In Fig. 4, a comparison between the ToF spectra of the mechanical and spin chopper can be seen. At longer wavelengths, the spin chopper appears to have a higher transmission compared to the mechanical chopper. Two factors are likely at play: first, as discussed previously, even though the active part of the spin chopper pulse consists of only seven cycles of a 1.4 MHz sine wave, the ringdown is considerably longer (25 μs). So the total signal length is approximately equal to the flight time through the RF coil for thermal neutrons. As a result, the TOF spectrum undersamples short wavelengths compared to long wavelengths. Second, the Fermi chopper exhibits a wavelength dependent transmission,[54] which may be approximated at long wavelengths by 1 minus the ratio between the channel width seen by a neutron of wavelength λ and the channel width when the chopper is at rest,

$$T = 1 - \frac{\omega m \lambda D^2}{4\pi d \hbar}, \tag{3}$$

where ω is the rotation frequency of the device, D is the length, and d is the width of the channels. Ideally, the transmission of the spin chopper would be independent of wavelength if the RF pulse time is much shorter than the flight time of the neutron through the RF coil. In this case, much like the double disk chopper,[55] the wavelength resolution is also wavelength independent, depending only on the distance between the chopper and the detector, L and the length of the RF coil D,

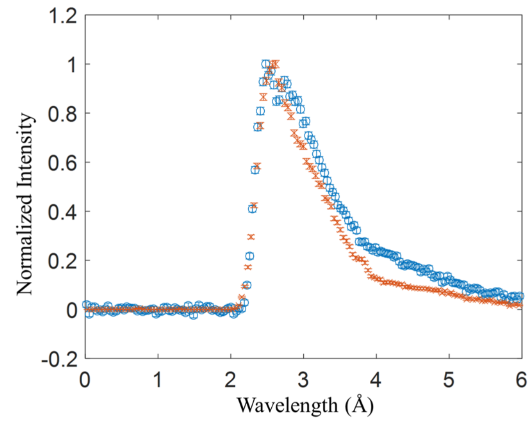

FIG. 4. Time of flight spectra produced using the RF spin chopping device (blue circular data points) and the mechanical chopper (orange cross shaped data points). The intensities shown are normalized to the maximum intensity.

$$\frac{\Delta\lambda}{\lambda} = \frac{D}{L}. \tag{4}$$

In addition, the RF pulse frequency may be tuned to optimize the available intensity for a given detector distance.

D. Spin echo small angle neutron scattering

Spin Echo Small Angle Neutron Scattering (SESANS) is an interferometric spin echo technique first designed to resolve small angle scattering smaller than the beam divergence.[33,34] In 2004, white beam spin echo was first explored in the context of pulsed TOF beams.[56] Later, the interferometric applications were further developed and applied to a variety of questions ranging from quantum contextuality[38,39] to (exotic[37]) gravity[36] and to probe properties of the neutron itself, such as the intrinsic coherence of a single neutron.[57] Regular spin echo uses two oppositely magnetized field regions, such that all precession induced in the first field region is reversed in the second, if the neutron velocity does not change in the instrument, i.e.,

$$\gamma B_1 \frac{L_1}{v_1} = -\gamma B_2 \frac{L_2}{v_2}, \tag{5}$$

where B is the magnetic field strength, L is the length of the precession region, and v is the neutron velocity. The index refers to the first or second precession region. Consequently, such a spin echo instrument is sensitive to small changes of the neutrons kinetic energy. In SESANS, the fields are applied over a rhombic region, such that refraction appears on the field borders (see Fig. 5). As a result, the instrument becomes sensitive to small changes in the neutrons transverse wavevector component, q (small angle scattering). If the velocity of the neutron is unchanged, the net phase accumulated by the neutron after a small angle scattering event is simply

$$\chi = \gamma B_2 \frac{\Delta L_2}{v}, \tag{6}$$

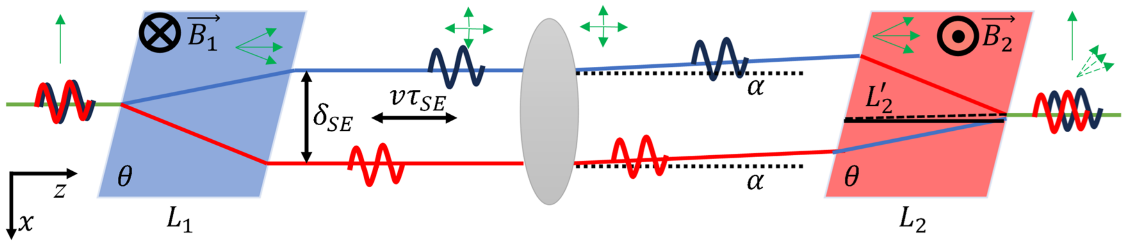

FIG. 5. Schematic representation of spin-echo small angle neutron scattering. Two inclined magnetic field regions of opposite polarization (represented in light blue and red) are used to induce a transverse separation between the two neutron spin states, also indicated in blue and red. The SESANS configuration shown here also induces a longitudinal separation between the wavepackets indicated by $v\tau_{SE}$. The sample indicated in gray causes the beam to be scattered by a small angle α. As a result, the path length through the second field region is changed to L_2' (as opposed to the non-scattered path L_2), resulting in a net phase shift between the two spin states upon recombination. A hypothetical neutron polarization is shown by the green arrow. The multiple arrows indicate dephasing. The final solid green arrow and dashed arrow represent the polarization of the unscattered and scattered beam, respectively.

where $\Delta L_2 = L_2' - L_2$ is the difference between the scattered and non-scattered neutron flight path length in the second arm, given by

$$\Delta L_2 = L_2 \cot(\theta_0)\alpha = L_2 \cot(\theta_0)\frac{q}{k}, \tag{7}$$

where α is the scattering angle and k is the neutron wavenumber $2\pi/\lambda$. Consequently, the phase is given by

$$\chi = \frac{\gamma m B_2 L_2 \cot(\theta_0)\lambda^2}{4\pi^2\hbar} q = \delta_{\mathrm{SE}}\, q, \tag{8}$$

where the spin-echo length δ_{SE} is equal to the induced transverse separation between the up and down spin state. The polarization is, therefore, a cosine transform of the scattering function $S(q)$,

$$P = \int dq \cos(\delta_{\mathrm{SE}} q) S(q) = G(\delta_{\mathrm{SE}}), \tag{9}$$

where $G(\delta_{\mathrm{SE}})$ is the real space correlation function. Since δ_{SE} is proportional to λ^2, a white beam SESANS, such as CANISIUS, averages over many different correlation lengths,

$$P = \frac{\int d\lambda G(\delta_{\mathrm{SE}}) I(\lambda)}{\int d\lambda I(\lambda)}, \tag{10}$$

where $I(\lambda)$ is the intensity distribution of the sampled beam. To extract the wavelength information, an additional precession coil (see nr. 5 in Fig. 1) can be used to measure the spin echo group [shown in Fig. 6(a)]. This precession coil adds a phase, which is field and wavelength dependent,

$$\varphi = \frac{\gamma B_p d m \lambda}{2\pi\hbar} = \kappa\lambda, \tag{11}$$

where d is the length of the precession coil and B_p is the field produced by said coil. Although it is practically more useful to think of $B_p d$ as the field integral produced by the coil, the field itself is not necessarily homogeneous across the neutron flight path. Hence, by adding the precession coil, the polarization becomes the cosine transform of the correlation function times the intensity distribution,

$$P(\kappa) = \frac{\int d\lambda G(\delta_{\mathrm{SE}}) I(\lambda) \cos(\kappa\lambda)}{\int d\lambda I(\lambda)}. \tag{12}$$

Consequently, the cosine transform of the polarization of the spin echo group, $P(\kappa)$, yields the correlation function weighted by the normalized intensity distribution. The correlation function of a specific sample can be extracted by normalizing the cosine transform of

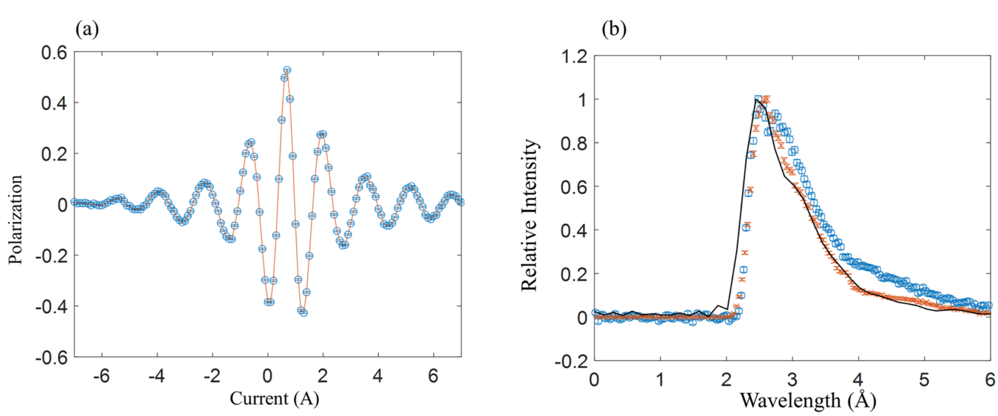

FIG. 6. (a) Polarization of the spin echo group measured against current in the precession coil. The individual data points with errorbars are shown in blue, while an interpolation of the data is shown in red. (b) The Fourier transform of the spin echo group is shown in black, while the spectra measured using both chopping techniques also shown in Fig. 4 are superposed. Note that no sample was inserted in the instrument for these measurements.

the spin echo group with sample, $P_1(\kappa)$ by a cosine transform of the spin echo group without the sample, $P_0(\kappa)$,

$$G(\delta_{\mathrm{SE}}) = \frac{\int d\kappa P_1(\kappa)\cos(\kappa\lambda)}{\int d\kappa P_0(\kappa)\cos(\kappa\lambda)}. \tag{13}$$

Since the correlation function of a vacuum is constant, the cosine transform of the spin echo group without a sample should simply be equal to the normalized spectrum. In Fig. 6, one can see the spin echo group measured by CANISIUS and its Fourier transform superposed on the normalized ToF spectra. Note that the maximal polarization of the spin echo group, roughly 0.6 is lower than the previously mentioned instrument polarization of 0.904. The latter is measured in non-precessing mode, where the neutron polarization is kept parallel or anti-parallel to the static fields supplied by the RF flipper magnets; however, the spin echo group is measured with the neutron polarization in the transverse plane (precessing mode). In this mode, the instrument is much more sensitive to spatial gradients in the field and also scattering from, for example, the wires in the field stepper. All of these factors contribute to the lower effective polarization observed in the spin echo group.

The spin echo length of CANISIUS was calibrated using a nanoporous alumina membrane from smartmembranes,[58] similar to the method described in Ref. 59. The pores used have a diameter of 40 nm, with a pitch of 125 nm and a thickness of 50 μm. A SEM image of the sample is shown in the inset of Fig. 7(a). Since the pitch of the pores is precisely known, we can use the measured SESANS correlation function to calibrate the spin echo length of CANISIUS. Note that the sample and sample holder confine the beam size to 7 × 10 mm^2. Figure 7(a) shows the correlation function measured using CANISIUS, as defined in Eq. (13), superposed on a predicted correlation function based on the phase object approximation.[60] The phase object approximation is used to calculate the SANS pattern produced by our sample, which, in turn, is Fourier transformed to obtain a van Hove correlation function $g(\delta_{\mathrm{SE}})$. Finally, we can convert this van Hove correlation function into a polarization ratio as described by Eq. (13), using the relation $G(\delta_{\mathrm{SE}}) = e^{\Sigma t(1-g(\delta_{\mathrm{SE}}))}$, with t being the sample thickness and Σ being the macroscopic scattering cross section. By making use of the phase object approximation, in particular, the SANS pattern, we can easily model the effect of instrument acceptance on the observed correlation function. The spin echo length axis of the CANISIUS measurement shown in in Fig. 7(a) has been scaled by a factor of 0.65 to overlap with the phase object approximation. Overlap between the white beam CANISIUS measurement and the estimate of the correlation function produced using phase object approximation demonstrates the feasibility of the white beam method detailed in this work. Our measurement shows that the spin echo length is shorter by a factor of 0.65 compared to the theoretical estimate based on the applied fields and distances. This discrepancy is most easily explained by the large stray fields between the RF flippers and the V-coils, which reduces the total amount of zero field precession. From this, the spin echo length range of CANISIUS at an RF frequency of 1.4 MHz is 70 nm < δ_{SE} < 300 nm.

To further confirm the reliability of the calibration sample, we measured the correlation function on Larmor at ISIS neutron source, a separate calibrated SESANS instrument.[61,62] The results are shown in Fig. 7(b). It can be seen that the period agrees well with the measurement conducted on the CANISIUS instrument. The difference in scaling is understood simply as arising from the different wavelength ranges and angular acceptances of each instrument. The locations of the correlation peaks do not yet agree. Hence, the calibration of the scaling and spin echo length ought to be further addressed in future work.

Apart from the fact that SESANS is not sensitive to collimation, the main advantage of white beam SESANS, exploited by CANISIUS, is the large available flux of a polychromatic beam compared to a monochromatic beam. This makes the method ideal at small neutron sources. White beam SESANS does, however, require careful calibration. First, the precession coil must be calibrated, which is important for extracting the Fourier transform variable κ [i.e., Eq. (11)]. This is required to properly convert the spin echo curves

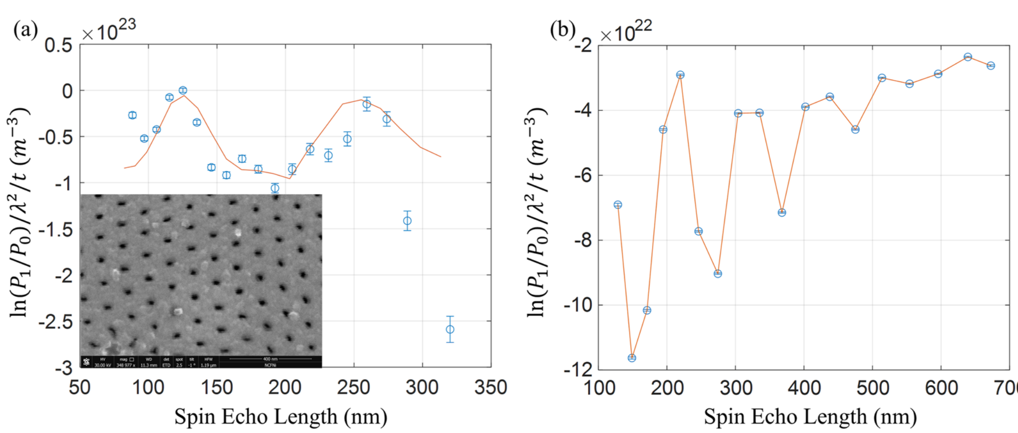

FIG. 7. (a) Normalized logarithm of the correlation function of the nanoporous sample measured using the white beam method on CANISIUS (blue) superposed on a fit function obtained using the phase object approximation. The inset shows an SEM image of the nanoporous alumina, carried out by USTEM at the TU Wien. (b) Normalized logarithm of the correlation function measured using the Larmor SESANS instrument at the ISIS neutron source[61] using the exact same sample. Note here that the red curve is not a phase object approximation but simply a trace of the data.

(polarization against coil current) into spectra. It can be accomplished by fitting the Fourier transform of the spin group to the measured spectrum of the beam. In addition to what is effectively a wavelength calibration, a spin echo length calibration is necessary. This is done, as shown in this section, using a calibration sample with known correlation lengths.

E. Coherent averaging

Constructing structured wavefunctions by coherent averaging is the main purpose of the CANISIUS instrument. This is done primarily to produce neutron wavefunctions that have non zero Orbital Angular Momentum (OAM) and to investigate the properties of these states. Put simply, coherent averaging is an interferometric technique that takes an input wavefunction with simple structure (i.e., Gaussian) and splits it multiple identical copies, called partial wavefunctions. These partial wavefunctions can then be independently translated and phase shifted in real or reciprocal space to produce a composite wavefunction (i.e., the coherent sum of all partial wavefunctions) that exhibits the desired structure. This technique is particularly well suited for producing neutron OAM, as explored in Refs. 15–17 and 63. Coherent averaging could be used to produce a circular array of partial wavefunctions, which act as coherent sources. If one can control the phase of each source, it becomes possible to produce arbitrary OAM values as described in Ref. 64. We have demonstrated the method previously in perfect crystal neutron interferometry.[16]

Since SESANS is also a type of neutron interferometer, it can be used to produce structured wavefunctions by coherent averaging. Here, the structured wave is produced by running the instrument in a new mode, where the first and second arms have different poleshoe angles. As a result, the two spin states retain some transverse separation after passing through the spin echo interferometer. The concept is illustrated in Fig. 8. This residual transverse separation is given by

$$\delta_{res} = \frac{\gamma m B \lambda^2}{4\pi^2\hbar}\left(\cot(\theta_1) - \cot(\theta_2)\right), \tag{14}$$

where we have assumed that $B = B_1 = B_2$ and $L = L_1 = L_2$. So for a Gaussian input wavefunction,

$$\psi_0 = Ae^{-x^2/\sigma^2}e^{ik_y y}, \tag{15}$$

where σ is the transverse coherence length. The transverse part of the output wavefunction after spin selection would be equal to

$$\psi_1 = \frac{A}{\sqrt{2}}\left(e^{i\beta/2}e^{-\frac{(x-\delta_{res}/2)^2-y^2}{\sigma^2}} + e^{-i\beta/2}e^{-\frac{(x+\delta_{res}/2)^2-y^2}{\sigma^2}}\right), \tag{16}$$

where β is a longitudinal phase between the two partial wavefunctions. β can be precisely tuned by changing the phase of one of the RF coils $\beta = 2\Delta\phi$. We can analyze the OAM or mode distribution by introducing the azimuthal Fourier transform,

$$\psi^{\ell}(r,z) = \frac{1}{2\pi}\int_0^{2\pi}\psi(r,\phi,z)e^{-i\ell\phi}d\phi, \tag{17}$$

and its inverse

$$\psi(r,\phi,z) = \sum_{\ell}\psi^{\ell}(r,z)e^{i\ell\phi}. \tag{18}$$

When we apply the azimuthal Fourier transform to our composite wavefunction, we find

$$\psi_1^{\ell}(r) = \sqrt{2}Ae^{-\frac{r^2+\delta_{res}^2/4}{\sigma^2}}J_{\ell}\left(i\frac{\delta_{res}}{\sigma^2}r\right)\cos\left(\frac{\pi\ell+\beta}{2}\right). \tag{19}$$

Since this mode amplitude is complex and spatially dependent, it can be useful to introduce a mode distribution function defined as

$$p[\ell] = 2\pi\int r|\psi^{\ell}(r)|^2 dr, \tag{20}$$

which is related to the OAM expectation value through

$$\langle\hat{L}_z\rangle = \hbar\sum_{\ell}\ell p[\ell]. \tag{21}$$

When we calculate the mode distribution function of (19), we find

$$p[\ell] = \frac{A^2\sigma^2}{2}e^{-\frac{\delta_{res}^2}{4\sigma^2}}I_{\ell}\left(\frac{\delta_{res}^2}{4\sigma^2}\right)|\cos|^2\left(\frac{\pi\ell+\beta}{2}\right). \tag{22}$$

We may now observe that for $\beta = 0$, $p[\ell]$ is only nonzero for even ℓ; that is, only the even OAM modes contribute to the output wavefunction, while for $\beta = \pi$, $p[\ell]$ is only nonzero for odd ℓ, and hence, only odd OAM modes contribute to the output wavefunction. By tuning the ratio δ_{res}/σ, we can determine how many modes contribute. For small splitting, only few modes contribute, whereas for

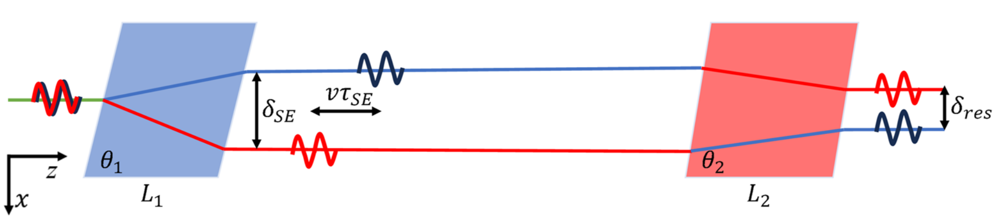

FIG. 8. Schematic representation of the coherent averaging mode of the CANISIUS instrument. This mode is almost equivalent to SESANS, the only difference being the different angles between the two field regions. This leads to an incomplete focusing of the two spin states, which is indicated by the residual distance δ_{res} between the states at the end of the instrument. Since the first arm also produces a longitudinal phase shift between the spin states, the second arm is necessary to preserve longitudinal coherence by canceling out this phase.

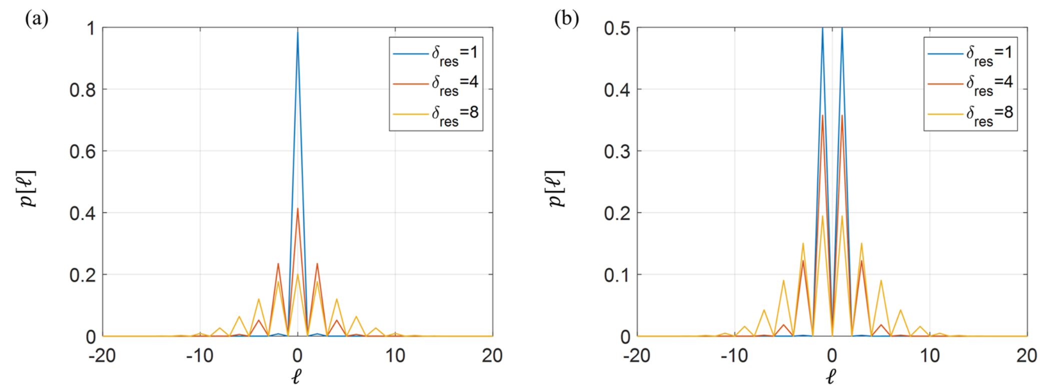

FIG. 9. OAM distribution function Eq. (22), in the special case where $\sigma = 1$ (a) $\beta = 0$ and (b) $\beta = \pi$ for various residual spin echo lengths δ_{res}. The OAM is measured around the propagation axis z. For both β, the OAM amplitude is non-zero only for every other mode. In (a), only even modes contribute, while in (b), only odd modes make up the wavefunction.

large splitting, many modes shape the wavefunction. Note that for CANISIUS, when θ_1 and θ_2 are set to 40° and 50°, respectively, we achieve a residual separation of 16–145 nm [see Eq. (14) and the spin echo scaling factor for CANISIUS of 0.65]. The transverse coherence scales with divergence and wavelength. For CANISIUS, we can calculate an approximate range of 40–120 nm, which is ideal for exploring the range around $\delta_{res}/\sigma = 1$. The OAM distribution function along with the aforementioned properties is shown in Fig. 9. Interestingly, we find that for $\beta = \pi$ and small δ_{res} with respect to the coherence length, the output wavefunction can almost entirely

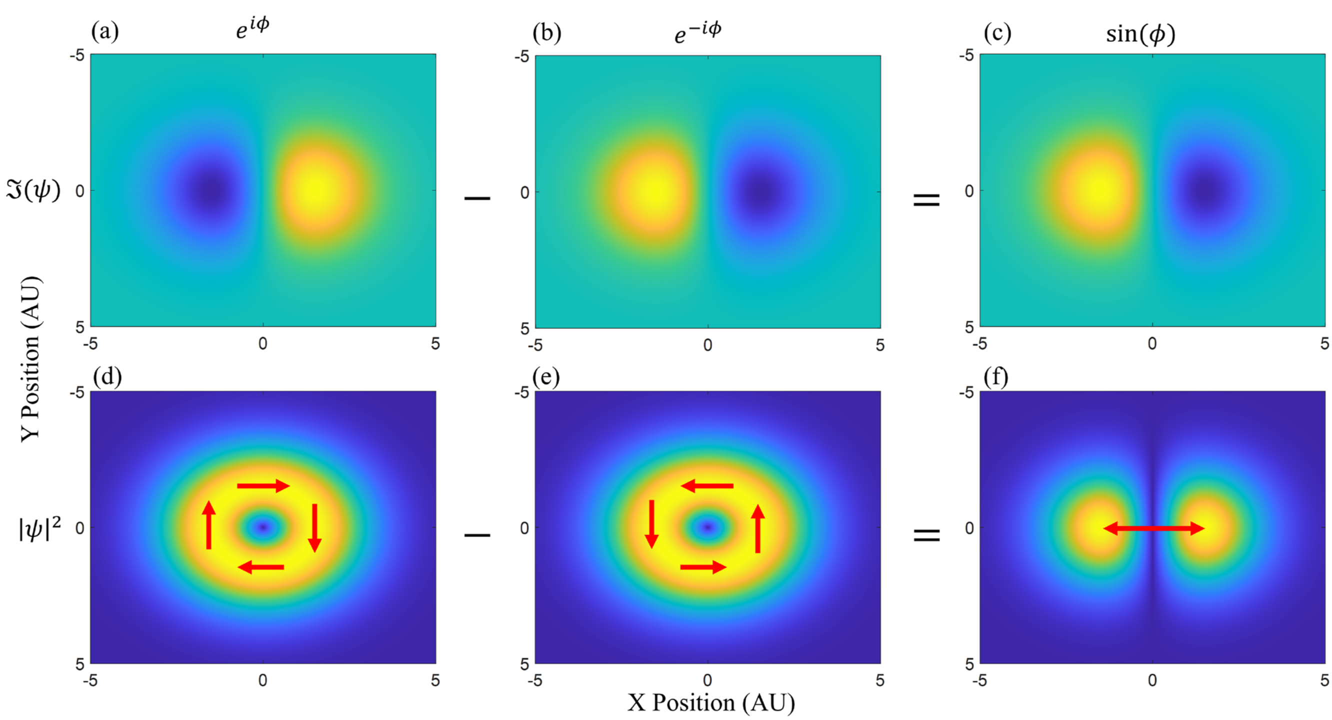

FIG. 10. Illustration of the construction of a linearly polarized OAM state. A clockwise rotating state (a)/(d) has a counter clockwise rotating state (b)/(e) subtracted from it, producing a linearly polarized state (c)/(f). The top insets (a)–(c) show the imaginary parts of the respective transverse wavefunction, while the bottom insets (d)–(f) show the absolute values, which is directly related to the expected intensity pattern. The red arrows indicate the local momentum, showing how the difference between the right and left rotating OAM modes produces a linear mode. The units on the x and y axes are arbitrary; however, for thermal neutrons with normal collimation, the transverse coherence is typically on the order of 10–200 nm.

be described by the $\ell = -1$ and $\ell = 1$ modes, i.e., a right and left twisting mode, somewhat analogous to linear polarization. The concept of a "linear" OAM state is illustrated in Fig. 10. Here, a left rotating state is subtracted from a right rotating state to produce a linearly polarized (sine oscillation) state. We have now shown that such a linearly polarized state can be approximated by a superposition of two Gaussian wavepackets with opposite amplitudes on opposite sides of the cylinder axis [Eq. (16)]. If δ_{res} is smaller than or on the order of σ, we find that Fig. 9 and Eq. (22) demonstrate that this very closely approximates a linearly polarized OAM state with $|\ell| = 1$. While this state has an average OAM of zero just like a pure $\ell = 0$ mode, it is orthogonal to a pure $\ell = 0$ state as nicely illustrated by looking at the OAM distribution function. In addition, even though the average OAM of each wavefunction produced by CANISIUS by coherent averaging is zero, the superpositions of $\ell = \pm 1$ or ± 2 are qualitatively different than the pure $\ell = 0$ mode, which are expected to scatter differently from nuclear targets.[22,23] In addition, the absorption characteristics of these states are expected to be different.[24] And as described in a recent paper, these states may be used to explore the quantum Sagnac effect,[65] where these superposition states may produce intensity beating proportional to the mode number and the rotation frequency of the observer. We propose that these linear OAM states that can be produced by CANISIUS and other SESANS instruments be used exactly to explore these differences in scattering and absorption cross sections in addition to the quantum Sagnac effect. Finally, since OAM is an additional quantum mechanical degree of freedom and the linear OAM state is orthogonal to the $\ell = 0$ state, we may use these states for experiments involving quantum information.

III. CONCLUSION

We have presented the new Austrian spin echo interferometer of the Atominstitut, CANISIUS, and illustrated its capabilities, both as a ToF and a broadband white beam instrument. In particular, we demonstrated the feasibility of polychromatic SESANS, which allows us to use the full potential of a continuous neutron source. This is especially important at weaker sources, such as the 250 kW TRIGA reactor at the Atominstitut. Finally, the coherent averaging capabilities of the instrument were illustrated. It was shown that CANISIUS is capable of producing neutrons that carry non zero OAM, in particular states that exist in a superposition of the $\ell = \pm 1$ modes. We expect this will be useful for exploring OAM dependent scattering and absorption cross sections, in addition to exploring fundamental aspects of quantum mechanics from the quantum Sagnac effect to quantum information and contextuality.

ACKNOWLEDGMENTS

N.G. and S.S. acknowledge funding from the Austrian Science Fund (FWF), DOI: 10.55776/P34239; For open access purposes, the author has applied a CC BY public copyright license to any author accepted manuscript version arising from this submission. In addition, N.G. is supported by the U.S. Department of Energy (DOE) Grant No. DE-SC0023695. The thermal white beam facility was designed, constructed, and funded by the Federal Ministry of Education, Science and Research of Austria. The 3D-design and development of CANISIUS were carried out by Roman Gergen. The authors are also grateful to the staff or the TRIGA center for making the beamtime available. Finally, the authors acknowledge and thank Wim Bouwman for useful discussion and resources regarding white beam SESANS.

AUTHOR DECLARATIONS

Conflict of Interest

The authors have no conflicts to disclose.

Author Contributions

Niels Geerits: Conceptualization (lead); Data curation (lead); Formal analysis (lead); Funding acquisition (supporting); Investigation (lead); Methodology (lead); Software (supporting); Writing – original draft (lead); Writing – review & editing (equal). **Simon Hack**: Data curation (supporting); Investigation (equal); Methodology (equal). **Lara Brukner**: Data curation (supporting); Investigation (equal); Methodology (equal). **Ad van Well**: Conceptualization (equal); Validation (supporting); Writing – review & editing (supporting). **Steven R. Parnell**: Data curation (supporting); Formal analysis (supporting); Investigation (supporting); Methodology (supporting); Writing – review & editing (equal). **Hartmut Abele**: Funding acquisition (supporting); Resources (lead). **Stephan Sponar**: Conceptualization (equal); Funding acquisition (lead); Project administration (lead); Resources (lead); Software (lead); Supervision (lead); Visualization (equal); Writing – original draft (equal); Writing – review & editing (equal).

DATA AVAILABILITY

The data that support the findings of this study are available from the corresponding author upon reasonable request.

REFERENCES

[1] Y. Hasegawa, R. Loidl, G. Badurek, M. Baron, and H. Rauch, "Violation of a Bell-like inequality in single-neutron interferometry," Nature **425**, 45–48 (2003).
[2] Y. Hasegawa, R. Loidl, G. Badurek, K. Durstberger-Rennhofer, S. Sponar, and H. Rauch, "Engineering of triply entangled states in a single-neutron system," Phys. Rev. A **81**, 032121 (2010).
[3] R. Colella, A. W. Overhauser, and S. A. Werner, "Observation of gravitationally induced quantum interference," Phys. Rev. Lett. **34**, 1472 (1975).
[4] G. Sagnac, "The demonstration of the luminiferous aether by an interferometer in uniform rotation," C. R. **157**, 708 (1913).
[5] S. A. Werner, J. L. Staudenmann, and R. Colella, "Effect of Earth's rotation on the quantum mechanical phase of the neutron," Phys. Rev. Lett. **42**, 1103–1106 (1979).
[6] B. Mashhoon, "Neutron interferometry in a rotating frame of reference," Phys. Rev. Lett. **61**, 2639–2642 (1988).
[7] A. Danner, B. Demirel, W. Kersten, H. Lemmel, R. Wagner, S. Sponar, and Y. Hasegawa, "Spin-rotation coupling observed in neutron interferometry," npj Quantum Inf. **6**, 23 (2020).
[8] R. Haun, F. E. Wietfeldt, M. Arif, M. G. Huber, T. C. Black, B. Heacock, D. A. Pushin, and C. B. Shahi, "Precision measurement of the neutron scattering length of ^{4}He using neutron interferometry," Phys. Rev. Lett. **124**, 012501 (2020).

[9]D. Sarenac, D. A. Pushin, M. G. Huber, D. S. Hussey, H. Miao, M. Arif, D. G. Cory, A. D. Cronin, B. Heacock *et al.*, "Three phase-grating moiré neutron interferometer for large interferometer area applications," Phys. Rev. Lett. **120**(11), 113201 (2018).
[10]I. Hidrovo, J. Dey, H. Meyer, D. S. Hussey, N. N. Klimov, L. G. Butler, K. Ham, and W. Newhauser, "Neutron interferometry using a single modulated phase grating," Rev. Sci. Instrum. **94**(4), 045110 (2023).
[11]F. Pfeiffer, C. Grünzweig, O. Bunk, G. Frei, E. Lehmann, and C. David, "Neutron phase imaging and tomography," Phys. Rev. Lett. **96**(21), 215505 (2006).
[12]C. Grünzweig, F. Pfeiffer, O. Bunk, T. Donath, G. Kühne, G. Frei, M. Dierolf, and C. David, "Design, fabrication, and characterization of diffraction gratings for neutron phase contrast imaging," Rev. Sci. Instrum. **79**(5), 053703 (2008).
[13]D. A. Pushin, D. Sarenac, D. S. Hussey, H. Miao, M. Arif, D. G. Cory, M. G. Huber, D. L. Jacobson, J. M. LaManna, J. D. Parker *et al.*, "Far-field interference of a neutron white beam and the applications to noninvasive phase-contrast imaging," Phys. Rev. A **95**(4), 043637 (2017).
[14]M. Bacak, J. Valsecchi, J. Čapek, E. Polatidis, A. Kaestner, A. Arabi-Hashemi, I. Kruk, C. Leinenbach, A. M. Long, A. Tremsin *et al.*, "Neutron dark-field imaging applied to porosity and deformation-induced phase transitions in additively manufactured steels," Mater. Des. **195**, 109009 (2020).
[15]D. Sarenac, D. G. Cory, J. Nsofini, I. Hincks, P. Miguel, M. Arif, C. W. Clark, M. G. Huber, and D. A. Pushin, "Generation of a lattice of spin-orbit beams via coherent averaging," Phys. Rev. Lett. **121**, 183602 (2018).
[16]N. Geerits, H. Lemmel, A.-S. Berger, and S. Sponar, "Phase vortex lattices in neutron interferometry," Commun. Phys. **6**, 209 (2023).
[17]D. Sarenac, C. Kapahi, W. Chen, C. W. Clark, D. G. Cory, M. G. Huber, I. Taminiau, K. Zhernenkov, and D. A. Pushin, "Generation and detection of spin-orbit coupled neutron beams," Proc. Natl. Acad. Sci. U. S. A. **116**, 20328–20332 (2019).
[18]Q. Le Thien, S. McKay, R. Pynn, and G. Ortiz, "Spin-textured neutron beams with orbital angular momentum," Phys. Rev. B **107**, 134403 (2023).
[19]C. W. Clark, R. Barankov, M. G. Huber, M. Arif, D. G. Cory, and D. A. Pushin, "Controlling neutron orbital angular momentum," Nature **525**, 504–506 (2015).
[20]D. Sarenac, M. E. Henderson, H. Ekinci, C. W. Clark, D. G. Cory, L. DeBeer-Schmitt, M. G. Huber, C. Kapahi, and D. A. Pushin, "Experimental realization of neutron helical waves," Sci. Adv. **8**, eadd2002 (2022).
[21]D. Sarenac, M. E. Henderson, H. Ekinci, C. W. Clark, D. G. Cory, L. DeBeer-Schmitt, M. G. Huber, O. Lailey, J. S. White, K. Zhernenkov, and D. A. Pushin, "Small-angle scattering interferometry with neutron orbital angular momentum states," Nat. Commun. **15**(1), 10785 (2024).
[22]A. V. Afanasev, D. V. Karlovets, and V. G. Serbo, "Schwinger scattering of twisted neutrons by nuclei," Phys. Rev. C **100**, 051601 (2019).
[23]A. V. Afanasev, D. V. Karlovets, and V. G. Serbo, "Elastic scattering of twisted neutrons by nuclei," Phys. Rev. C **103**, 054612 (2021).
[24]T. Jach and J. Vinson, "Method for the definitive detection of orbital angular momentum states in neutrons by spin-polarized ^{3}He," Phys. Rev. C **105**, L061601 (2022).
[25]H. Rauch, W. Treimer, and U. Bonse, "Test of a single crystal neutron interferometer," Phys. Lett. A **47**, 369–371 (1974).
[26]T. Fujiie, M. Hino, T. Hosobata, G. Ichikawa, M. Kitaguchi, K. Mishima, Y. Seki, H. M. Shimizu, and Y. Yamagata, "Development of neutron interferometer using multilayer mirrors and measurements of neutron-nuclear scattering length with pulsed neutron source," Phys. Rev. Lett. **132**, 023402 (2024).
[27]R. Gähler, R. Golub, K. Habicht, T. Keller, and J. Felber, "Space-time description of neutron spin echo spectrometry," Physica B **229**, 1–17 (1996).
[28]F. Mezei, "Neutron spin echo: A new concept in polarized thermal neutron techniques," Z. Phys. A **255**, 146–160 (1972).
[29]R. Golub and R. Gähler, "A neutron resonance spin echo spectrometer for quasi-elastic and inelastic scattering," Phys. Lett. A **123**, 43–48 (1987).
[30]R. Gähler, R. Golub, and T. Keller, "Neutron resonance spin echo—A new tool for high resolution spectroscopy," Physica B **180–181**, 899–902 (1992).
[31]S. Sponar, J. Klepp, C. Zeiner, G. Badurek, and Y. Hasegawa, "Violation of a Bell-like inequality for spin-energy entanglement in neutron polarimetry," Phys. Lett. A **374**, 431–434 (2010).
[32]J. C. Leiner, S. J. Kuhn, S. McKay, J. K. Jochum, F. Li, A. A. M. Irfan, F. Funama, D. Mettus, L. Beddrich, C. Franz, J. Shen, S. R. Parnell, R. M. Dalgliesh, M. Loyd, N. Geerits, G. Ortiz, C. Pfleider, and R. Pynn, "Spin-energy entanglement of a time-focused neutron," Phys. Rev. Applied **22**, L031005 (2024).
[33]R. Pynn, "Neutron spin-echo and three-axis spectrometers," J. Phys. E **11**, 1133 (1978).
[34]M. T. Rekveldt, "Novel SANS instrument using neutron spin echo," Nucl. Instrum. Methods Phys. Res., Sect. B **114**, 366–370 (1996).
[35]M. T. Rekveldt, W. G. Bouwman, W. H. Kraan, T. V. Krouglov, and J. Plomp, "Larmor precession applications: Magnetised foils as spin flippers in spin-echo SANS with varying wavelength," Physica B **335**, 164–168 (2003).
[36]V.-O. de Haan, J. Plomp, A. A. van Well, M. T. Rekveldt, Y. H. Hasegawa, R. M. Dalgliesh, and N.-J. Steinke, "Measurement of gravitation-induced quantum interference for neutrons in a spin-echo spectrometer," Phys. Rev. A **89**, 063611 (2014).
[37]S. R. Parnell, A. A. van Well, J. Plomp, R. M. Dalgliesh, N.-J. Steinke, J. F. K. Cooper, N. Geerits, K. E. Steffen, W. M. Snow, and V. O. de Haan, "Search for exotic spin-dependent couplings of the neutron with matter using spin-echo based neutron interferometry," Phys. Rev. D **101**, 122002 (2020).
[38]J. Shen, S. J. Kuhn, R. M. Dalgliesh, V. O. de Haan, N. Geerits, A. A. M. Irfan, F. Li, S. Lu, S. R. Parnell, J. Plomp, A. A. van Well, A. Washington, D. V. Baxter, G. Ortiz, W. M. Snow, and R. Pynn, "Unveiling contextual realities by microscopically entangling a neutron," Nat. Commun. **11**, 930 (2020).
[39]S. J. Kuhn, S. McKay, J. Shen, N. Geerits, R. M. Dalgliesh, E. Dees, A. A. M. Irfan, F. Li, S. Lu, V. Vangelista, D. V. Baxter, G. Ortiz, S. R. Parnell, W. M. Snow, and R. Pynn, "Neutron-state entanglement with overlapping paths," Phys. Rev. Res. **3**, 023227 (2021).
[40]R. M. Dalgliesh, S. Langridge, J. Plomp, V. O. de Haan, and A. A. van Well, "Offspec, the ISIS spin-echo reflectometer," Physica B **406**, 2346–2349 (2011).
[41]N. Geerits, S. R. Parnell, M. A. Thijs, A. A. van Well, C. Franz, A. L. Washington, D. Raspino, R. M. Dalgliesh, and J. Plomp, "Time of flight modulation of intensity by zero effort on Larmor," Rev. Sci. Instrum. **90**, 125101 (2019).
[42]N. Geerits, S. R. Parnell, M. A. Thijs, W. G. Bouwman, and J. Plomp, "Applying resonant spin flippers with poleshoes and longitudinal radio frequency fields to time of flight MIEZE," J. Phys.: Conf. Ser. **1316**, 012011 (2019).
[43]M. T. Rekveldt, J. Plomp, W. G. Bouwman, W. H. Kraan, S. Grigoriev, and M. Blaauw, "Spin-echo small angle neutron scattering in Delft," Rev. Sci. Instrum. **76**, 033901 (2005).
[44]A. N. Bazhenov, V. M. Lobashev, A. N. Pirozhkov, and V. N. Slusar, Nucl. Instrum. Methods Phys. Res., Sect. A **332**, 534–536 (1993).
[45]F. Li, S. R. Parnell, H. Bai, W. Yang, W. A. Hamilton, B. B. Maranville, R. Ashkar, D. V. Baxter, J. T. Cremer, and R. Pynn, "Spin echo modulated small-angle neutron scattering using superconducting magnetic Wollaston prisms," J. Appl. Crystallogr. **49**, 55–63 (2016).
[46]H. Rauch, J. Harms, and H. Moldaschl, "A neutron spin-flip chopper for the time-of-flight measurements," in *Neutron Inelastic Scattering Vol. II. Proceedings of a Symposium on Neutron Inelastic Scattering* (1968), pp. 387–394.
[47]H. Freisleben and H. Rauch, "Neutron spin-flip-chopper with high repetition rates," Nucl. Instrum. Methods **98**, 61–67 (1972).
[48]Swissneutronics, 2025, https://swissneutronics.ch/portfolio/supermirrors-en/.
[49]S. V. Grigoriev, R. Kreuger, W. H. Kraan, F. M. Mulder, and M. T. Rekveldt, "Neutron wave-interference experiments with adiabatic passage of neutron spin through resonant coils," Phys. Rev. A **64**, 013614 (2001).
[50]H. Rauch, H. Wölwitsch, H. Kaiser, R. Clothier, and S. A. Werner, "Measurement and characterization of the three-dimensional coherence function in neutron interferometry," Phys. Rev. A **53**, 902–908 (1996).
[51]F. Li, R. Dadisman, and D. C. Wasilko, "Optimization of a superconducting adiabatic radio frequency neutron resonant spin flipper," Nucl. Instrum. Methods Phys. Res., Sect. A **955**, 163300 (2020).
[52]J. Plomp, "Spin-echo development for a time-of-flight neutron reflectometer," Ph.D. thesis, Universal Press, 2009.
[53]W. C. Chen, R. Erwin, P. Tsai, M. T. Hassan, N. Hadad, and C. F. Majkrzak, "A large beam high efficiency radio frequency neutron spin flipper," Rev. Sci. Instrum. **92**, 063906 (2021).

[54]E. Fermi, J. Marshall, and L. Marshall, "A thermal neutron velocity selector and its application to the measurement of the cross section of boron," Phys. Rev. **72**, 193–196 (1947).
[55]A. A. van Well and H. Fredrikze, "On the resolution and intensity of a time-of-flight neutron reflectometer," Physica B **357**, 204–207 (2005).
[56]W. G. Bouwman, W. Stam, T. V. Krouglov, J. Plomp, S. V. Grigoriev, W. H. Kraan, and M. T. Rekveldt, "SESANS with a monochromatic beam or with time-of-flight applied on colloidal systems," Nucl. Instrum. Methods Phys. Res., Sect. A **529**(1–3), 16–21 (2004).
[57]S. McKay, A. A. M. Irfan, Q. Le Thien, N. Geerits, S. R. Parnell, R. M. Dalgliesh, N. V. Lavrik, I. I. Kravchenko, G. Ortiz, and R. Pynn, "Experimental evidence for the two-path description of neutron spin echo," Phys. Rev. A **109**, 042420 (2024).
[58]Smartmembranes, 2024, http://www.smartmembranes.de/en/products/nanoporous-alumina/.
[59]F. Funama, C. M. Wolf, K. Weigandt, J. Shen, S. R. Parnell, and F. Li, "Spin echo small-angle neutron scattering using superconducting magnetic Wollaston prisms," Rev. Sci. Instrum. **95**, 073709 (2024).
[60]V. O. Haan, J. Plomp, W. G. Bouwman, M. Trinker, T. M. Rekveldt, C. P. Duif, E. Jericha, H. Rauch, and A. A. Van Well, "Phase-object approximation in small-angle neutron scattering experiments on silicon gratings," J. Appl. Crystallogr. **40**(1), 151–157 (2007).
[61]G. Smith, "Reproducibility measurement of flexipor membrane using LARMOR SESANS system," STFC ISIS Neutron and Muon Source (2023).
[62]F. Funama, G. N. Smith, S. R. Parnell, C. P. Duif, W. G. Bouwman, R. Pynn, R. M. Dalgliesh, and F. Li, "Data reproducibility of spin-echo small-angle neutron scattering instruments," Neutron News **36**(1), 9–12 (2025).
[63]D. Sarenac, J. Nsofini, I. Hincks, M. Arif, C. W. Clark, D. G. Cory, M. G. Huber, and D. A. Pushin, "Methods for preparation and detection of neutron spin-orbit states," New J. Phys. **20**, 103012 (2018).
[64]H. Wang and A. Afanasev, "Topology and polarization of optical vortex fields from atomic phased arrays," Appl. Sci. **13**(9), 5672 (2023).
[65]N. Geerits, S. Sponar, K. E. Steffen, W. M. Snow, S. R. Parnell, G. Mauri, G. N. Smith, R. M. Dalgliesh, and V. de Haan, "Measuring the angular momentum of a neutron using Earth's rotation," Phys. Rev. Res. **7**, 013046 (2025).